

REGULAR PAPER

SiC nano-dot formation in bulk-Si substrate using hot-C⁺-ion implantation process

To cite this article: Tomohisa Mizuno *et al* 2019 *Jpn. J. Appl. Phys.* **58** 081004

View the [article online](#) for updates and enhancements.



SiC nano-dot formation in bulk-Si substrate using hot-C⁺-ion implantation process

Tomohisa Mizuno^{1*}, Masaki Yamamoto¹, Shinji Nakada¹, Sho Irie¹, Takashi Aoki¹, and Toshiyuki Sameshima²¹Department of Science, Kanagawa University, Hiratsuka, Kanagawa 259-1293, Japan²Department of Engineering, Tokyo University of Agriculture and Technology, Koganei, Tokyo 184-8588, Japan*E-mail: mizuno@kanagawa-u.ac.jp

Received March 31, 2019; revised June 15, 2019; accepted June 18, 2019; published online July 12, 2019

We experimentally studied SiC nano-dot formation in a bulk-Si substrate fabricated by the very simple processes of a hot-C⁺-ion implantation into (100) bulk-Si substrate and the following N₂-annealing, and the photoluminescence (PL) properties for a future Si-based photonic device. We confirmed by a transmission electron microscope that cubic and hexagonal SiC dots are formed in a C⁺-ion implanted Si layer, and the SiC dot diameter (3–7 nm) and density (1–2 × 10¹² cm⁻²) depend on the process conditions. We also observed very strong PL-intensity after N₂-annealing, and the broad PL spectrum can be fitted by the sum of the PL-emissions from four different cubic and hexagonal SiC-polytypes with different exciton bandgaps. The PL-properties strongly depend on the N₂-annealing temperature, and hot-C⁺-ion implantation temperature and dose. Consequently, we successfully optimize the process conditions to improve PL-intensity, as well as to control the PL-spectrum line shape in the near-UV/visible regions. © 2019 The Japan Society of Applied Physics

1. Introduction

A two-dimensional (2D) Si layer is one of the key structures for realizing both Si-based photonic^{1–3)} and CMOS devices, because the high quantum confinement effect of electrons in 2D-Si^{4–13)} can modulate 2D-Si crystals into a direct-bandgap material from an indirect-bandgap three-dimensional (3D) Si.^{2,10,14,15)} However, the bandgap E_G and the peak photoluminescence (PL) photon wavelength λ_{PL} of (100) 2D-Si are still lower than 1.9 eV and longer than 650 nm, respectively, and the PL intensity I_{PL} is too low for the Si-based visible-photonic devices.^{9,14)} Therefore, it is strongly required to study a Si-based-semiconductor with higher E_G , such as 3D Si_{1-y}C_y whose E_G and a PL intensity increase with increasing y .^{16–18)} Moreover, silicon carbide (SiC) nanostructures, such as a porous-SiC,^{19–22)} 2D-SiC,^{19,23,24)} SiC-nanowire,^{19,25)} and SiC-dot,^{19,26,27)} are widely studied. There are many diverse polytypes in SiC structures whose physical properties including E_G also depend on the polytype and the dimensions of SiC.^{19,28)} It is also reported that 3D-SiC can emit the PL photons by many recombination processes, such as, free exciton recombination,^{19,28,29)} except band to band recombination, although 3D-SiC has an indirect-bandgap structure.^{19,28)} Therefore, the PL peak energy E_{PH} of 3D-SiC is equal to the exciton gap energy E_{GX} which is approximately 0.1 eV lower than E_G .^{19,28)}

Recently, we have experimentally studied a Si_{1-y}C_y layer fabricated by hot-¹²C⁺-ion implantation into a (100) SOI with an approximately 100 nm thick surface oxide (SOX) at a high substrate temperature T and heavy C⁺ ion dose D_C in the wide range of 500 °C ≤ T ≤ 1000 °C, 5 × 10¹² ≤ D_C ≤ 7 × 10¹⁶ cm⁻² (0.01 < y ≤ 0.3), and 0.5 ≤ d_s ≤ 20 nm.^{30–33)} According to the self-cluster effects of ion implanted C atoms with the C cluster size of several nm in a crystal-Si (c-Si) layer^{33–35)} analyzed by atom probe tomography (ATP), C content in the c-Si locally condenses both at the SOX/Si and buried-oxide (BOX)/Si interfaces in c-Si layer, which leads to the local formation of SiC dots in c-Si.^{30–33)} The hot-C⁺-ion implantation process can reduce the ion implantation induced damage of the Si layer.³¹⁾ Under a heavy C dope condition of higher than 2 × 10¹⁶ cm⁻², X-ray photoelectron spectroscopy (XPS)

and ATP showed that C atoms segregate with an approximately 2 nm thickness at both the SOX/Si and BOX/Si interfaces.^{31–33)} In addition, the ATP analysis for 3D distribution of C atoms evaluated that C atoms clustered both in Si layer and the C segregation layer near the oxide/Si interfaces.^{32,33)} As a result, the partial formation of cubic (3C-SiC) and hexagonal SiC (H-SiC) nano-dots was confirmed at both the SOX/Si and the BOX/Si interfaces, using corrector-spherical aberration transmission electron microscopy (CSTEM) and electron diffraction (ED) patterns that were obtained by fast Fourier transform (FFT) analysis of the lattice spots of CSTEM data.^{32,33)} We also demonstrated very large E_{PH} (≈3 eV) and very high PL intensities (I_{PL}) from the near-UV to visible regions (>350 nm) of SiC dots, which markedly increase with increasing the C content in Si layer. Very high PL emission, which is about 100 times higher than that from 2D-Si,³¹⁾ originates from the SiC dots in the C segregation layer at the SOX/Si and BOX/Si interfaces.^{31–33)} PL intensity and peak PL energy (E_{PH}) strongly depend on T and D_C , and we can successfully optimize T and D_C to improve I_{PL} .^{32,33)} Moreover, even in an amorphous-Si and poly-Si substrates as well as in a bulk-Si substrate, SiC nano-dots were successfully formed and the strong PL emission was observed.^{36–38)} Thus, the hot-¹²C⁺-ion implantation technique, which is a compatible ULSI process, is highly suitable for visible-region Si-based photonic devices,¹⁾ and as well as for electron and photonic hybrid devices in ULSI.³⁰⁾

In this work, we experimentally studied the process condition dependence (hot-¹²C⁺-ion implantation temperature T , C⁺ ion dose D_C , and N₂ annealing temperature T_N) of physical properties of SiC nano-dots in a (100) bulk-Si in detail,^{36,37)} which was fabricated by the self-cluster effects of C atoms in hot-¹²C⁺-ion implanted bulk-Si layer (C⁺-bulk Si). We analyzed the material structures and PL properties of SiC dots, using, XPS, CSTEM, ED pattern of lattice spots of SiC dots. CSTEM and ED analyzes showed that 3C- and H-SiC dots with a diameter of approximately 2 nm grow into the SOX layer from the surface Si, and are also formed with a relatively large diameter of approximately 5 nm in the surface bulk-Si layer with the average C content higher than 4 at%. We confirmed very strong PL emission from the SiC

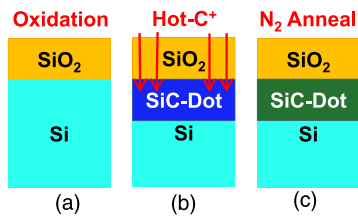


Fig. 1. (Color online) Schematic fabrication steps for SiC dots in bulk-Si. After thermal dry oxidation of Si ($T_{OX} \approx 100$ nm) at 1000°C (a), (b) shows that hot- C^+ -ions were implanted into a (100) bulk-Si substrate for forming SiC dots at the Si substrate temperature T . (c) shows that post N_2 annealing was carried out in various T_N for t_N after (a) and (b) steps, to reduce the C^+ ion implantation induced damage in Si layer.

nano-dots in the wide range of near-UV/visible regions. Moreover, the PL properties of SiC dots strongly depend on both T , D_C and T_N .

2. Experimental procedure

Figure 1 shows the schematic fabrication steps of SiC nano-dots in a (100) bulk-Si substrate. As shown in Fig. 1(b), SiC dots were fabricated by hot- C^+ -ion implantation into the (100) bulk-Si substrate (C^+ -bulk-Si) at various substrate temperature T after forming an approximately 100 nm thick SOX, as shown in Fig. 1(a).³⁶⁾ In this study, T was varied from 25°C to 900°C , and $1 \times 10^{16} \leq D_C \leq 6 \times 10^{16} \text{cm}^{-2}$, where the C^+ ion energy $E_A = 30$ keV whose projection range was set to be the Si surface. The hot- C^+ -ion implantation time is proportional to C^+ ion dose, and was approximately 2.5 h at $D_C = 4 \times 10^{16} \text{cm}^{-2}$. Figure 1(c) shows that a post N_2 annealing at various T_N for an annealing time t_N was also carried out to recover the C^+ ion implantation induced damage of Si under the T_N conditions of $500^\circ\text{C} \leq T_N \leq 1200^\circ\text{C}$. 20 nm thick SOI substrate was also fabricated (C^+ -SOI) by the same process conditions of hot- C^+ -ion implantation in C^+ -bulk-Si, as a reference.

The material structures of the SiC dots was evaluated by CSTEM and the ED patterns obtained by FFT analysis of the lattice spots of CSTEM. The C content Y depth profile was evaluated by the C1s spectrum of XPS whose accuracy was ± 1 at%³¹⁾ PL properties were measured at room temperature, where the excitation He-Cd laser energy E_{EX} was 3.8 eV, the laser power was approximately 0.6 mW, and the laser diameter was $1 \mu\text{m}$. At $E_{EX} = 3.8$ eV, the PL photons were mainly emitted from the SiC nano-dots near the SOX/Si interface, because the photon penetration length λ_{EX} of 3.8 eV laser in Si layer is only 8 nm.^{31,39)} The PL spectrum in the wide range of photon wavelengths λ_{PL} from the UV to NIR region was calibrated using a standard illuminant.³¹⁾ Moreover, the PL intensity variation within about 1cm^2 area of Si substrate under each process condition was approximately $\pm 10\%$. On the other hand, the accuracy of the peak PL energy E_{PH} obtained by fitting the measured PL spectrum was estimated to be approximately ± 0.04 eV, because of the broad PL spectrum. On the other hand, the phonon properties of C^+ -Si layer by Si-Si vibration Raman spectroscopy were measured at room temperature, where the excitation He-Cd laser length λ_{EX} condition was 325 nm, the laser power was approximately 0.6 mW, and the laser diameter was $1 \mu\text{m}$. However, the Raman intensity of Si-C vibration of SiC dots (TO mode around 780cm^{-1}) was too low to evaluate the

crystal quality of SiC dots in detail,³⁸⁾ because of small total area of SiC dots. Thus, in this study, the crystal quality of SiC dots is indirectly evaluated by the Raman properties of C^+ Si layer.³⁸⁾

3. Results and discussion

3.1. SiC nano-dot formation in C^+ -bulk-Si

Figures 2(a) and 2(b) show the T dependence of C content depth profiles of Si-C bond evaluated by XPS analysis (C1s spectrum) before and after N_2 annealing, respectively, where $D_C = 4 \times 10^{16} \text{cm}^{-2}$. Solid and dotted lines in Fig. 2(a) before N_2 annealing show the data at $T = 25^\circ\text{C}$ and 600°C before N_2 annealing, respectively, and the C content profile is almost independent of T . After N_2 annealing, solid line in Fig. 2(b) shows the data at $T = 600^\circ\text{C}$, $T_N = 1000^\circ\text{C}$ and $t_N = 5$ min, and dotted line in Fig. 2(b) shows the data at $T = 800^\circ\text{C}$, $T_N = 900^\circ\text{C}$ and $t_N = 10$ min. Figures 2(a) and 2(b) show that the C content of Si-C bonds is higher than 10 at% within 30 nm depth from the Si surface. This relatively broad C content depth profile is the characteristic of C^+ -bulk-Si, which is much different from that of C^+ -SOI at $T = 800^\circ\text{C}$ that has the large C segregation effects at both SOX/Si and BOX/Si interfaces,³³⁾ and thus, the peak C content of Si-C bonds of C^+ -bulk-Si (=13 at%) is about one half of that of C^+ -SOI (=25 at%).³³⁾ Figure 2(b) shows that the C content profile near the Si surface region is redistributed after short N_2 annealing, resulting in the peak C content around 10 nm from the Si surface. In addition, after short N_2 annealing, the C content profile of Si-C bond is almost the same as the data at $T = 800^\circ\text{C}$ shown in Fig. 2(b), which also indicates that the C content profile of Si-C bond after short N_2 annealing is almost independent of T . Thus, Figs. 2(a) and 2(b) data indicate that the C content of Si-C bond can be controlled by D_C and N_2 annealing. Consequently, the C content of Si-C bond is almost independent of T and N_2 annealing, but the C content at the SOX/Si interface and peak C content in the Si layer is partially affected by both the T increase and N_2 annealing. The C atoms are segregated at the SOX/Si interface in a C^+ -bulk-Si under $T \geq 600^\circ\text{C}$ and the segregation effect is enhanced with increasing T . In summary, Fig. 2(c) shows the T dependence of the peak C content of Si-C bond at the SOX/Si interface (C segregation area). Squares and circles show the data before and after N_2 annealing, respectively. The peak C content of Si-C bond in the C segregation area depends on T and rapidly increases with T increasing under $T \geq 600^\circ\text{C}$, but the peak C content at $T = 600^\circ\text{C}$ is not affected by N_2 annealing.

On the other hand, Fig. 3 shows the T dependence of C content depth profiles of C-C bond evaluated by XPS analysis (C1s spectrum), where $D_C = 4 \times 10^{16} \text{cm}^{-2}$. Dashed and dotted lines show the data at $T = 600^\circ\text{C}$ and 25°C before N_2 annealing, respectively, and solid line shows the data at $T = 600^\circ\text{C}$, $T_N = 1000^\circ\text{C}$ and $t_N = 5$ min, respectively. The low C content of C-C bond (1–2 at%) was observed only in SOX layer and thus, some C atoms are separated out only in oxide layer. The C content of C-C bond depends on T , but is independent of N_2 annealing.

Next, we discuss the SiC dot structure. Figures 4(a) and 4(b) show TEM images of the cross section of the surface Si layers before and after N_2 annealing at $T_N = 1000^\circ\text{C}$

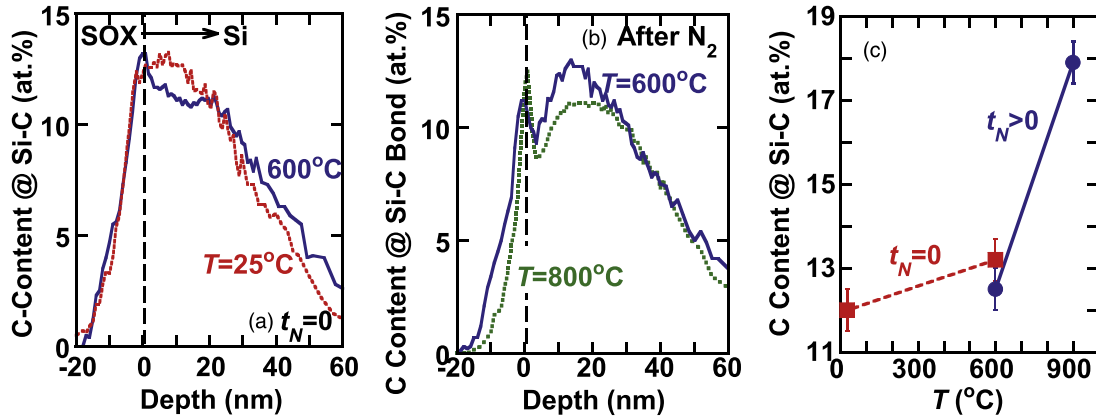


Fig. 2. (Color online) T dependence of C content depth profiles of Si-C bond evaluated by XPS analysis (C1s spectrum) (a) before and (b) after N_2 annealing, where $D_C = 4 \times 10^{16} \text{ cm}^{-2}$. Solid and dotted lines in (a) show the data at $T = 25^\circ\text{C}$ and 600°C before N_2 annealing, respectively. Solid line in (b) shows the data at $T = 600^\circ\text{C}$, $T_N = 1000^\circ\text{C}$ for $t_N = 5 \text{ min}$, and dotted line in (b) shows the data at $T = 800^\circ\text{C}$, $T_N = 900^\circ\text{C}$ for $t_N = 10 \text{ min}$. (b) shows that the C content of Si-C bond is almost independent of T and N_2 annealing, but the C content at the SOX/Si interface and peak C content in the Si layer is partially affected by N_2 annealing. (c) T dependence of the peak C content of Si-C bond at the Si surface (C segregation area) evaluated by XPS analysis (C1s spectrum), where $D_C = 4 \times 10^{16} \text{ cm}^{-2}$. Squares and circles show the data before and after N_2 annealing shown in Figs. 2(a) and 2(b), respectively. The peak C content of Si-C bond at the SOX/Si interface depends on T and rapidly increases with increasing T under $T \geq 600^\circ\text{C}$.

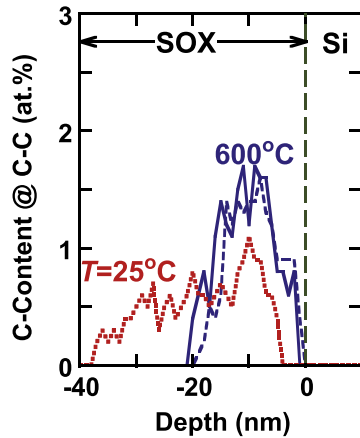


Fig. 3. (Color online) T dependence of C content depth profiles of C-C bond evaluated by XPS analysis (C1s spectrum), where $D_C = 4 \times 10^{16} \text{ cm}^{-2}$. Dashed, dotted, and solid lines show the data at $T = 600^\circ\text{C}$, 25°C before N_2 annealing, and at $T = 600^\circ\text{C}$, $T_N = 1000^\circ\text{C}$ for $t_N = 5 \text{ min}$, respectively. C atoms are separated out only in SOX layer. The C content of C-C bond in SOX layer depends on T , but is independent of N_2 annealing.

for $t_N = 5 \text{ min}$, respectively, where $T = 600^\circ\text{C}$ and $D_C = 4 \times 10^{16} \text{ cm}^{-2}$. Many SiC dots, shown as white dot areas pointed out by arrows, successfully formed within approximately 50 nm depth from the Si surface whose C content is higher than 4 at% shown in Fig. 2(b). However, Fig. 4(b) shows that the SiC dot size decreases after N_2 annealing, compared to the SiC dot size of Fig. 4(a) before N_2 annealing. Moreover, Si layer under the SiC dot formation layer in Fig. 4(a) shows many dislocations pointed out by arrow (dislocation layer), which are possibly attributable to the Si lattice mismatch between the SiC dot layer with relatively small lattice constant by SiC dot formation and relaxed bulk-Si substrate. However, Fig. 4(b) shows that the dislocations drastically decrease after N_2 annealing, which is possibly attributable to the SiC dot layer relaxation by high temperature N_2 annealing.

Firstly, we discuss SiC dot properties in C^+ -Si layer, where $D_C = 4 \times 10^{16} \text{ cm}^{-2}$. In order to evaluate the T dependence of the SiC dot size R and density N , Figs. 5(a)

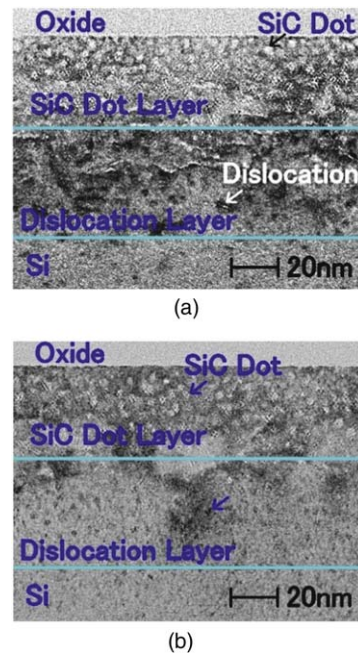


Fig. 4. (Color online) TEM images of the cross section of the surface C^+ Si layers at (a) $t_N = 0$ and (b) $t_N = 5 \text{ min}$, where $T = 600^\circ\text{C}$, $T_N = 1000^\circ\text{C}$, and $D_C = 4 \times 10^{16} \text{ cm}^{-2}$. Many SiC dots, pointed out by arrows, successfully formed within approximately 50 nm depth from the Si surface before and after N_2 annealing. However, (b) shows that the SiC dot size decreases after N_2 annealing, compared to the SiC dot size before N_2 of (a). Moreover, as shown in (a), Si layer under the SiC dot formation layer shows many dislocations, but (b) shows that the dislocations are recovered after N_2 annealing.

and 5(b) show TEM images of the cross section of Si layer before N_2 annealing at $T = 25^\circ\text{C}$ and 600°C , respectively. White round regions pointed by arrows show SiC dots. Figure 5(a) even at $T = 25^\circ\text{C}$ shows that some SiC dots with the R of an approximately 1–1.5 nm can be observed within an approximately 10 nm depth from the Si surface, but the SiC dot shape is obscure and the density is very low, compared to Fig. 5(b) at $T = 600^\circ\text{C}$. Thus, it is difficult to evaluate the N at room temperature C^+ ion implantation. However, Fig. 5(b) at high $T = 600^\circ\text{C}$ shows that many SiC

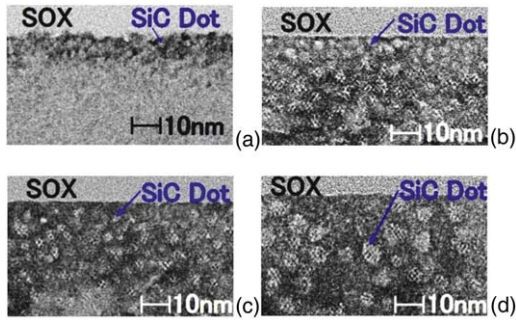


Fig. 5. (Color online) CSTEM images of SiC dots as the function of process conditions, where $D_C = 4 \times 10^{16} \text{ cm}^{-2}$. (a) $T = 25 \text{ }^\circ\text{C}$ and (b) $T = 600 \text{ }^\circ\text{C}$ before N_2 annealing. (c) $T = 600 \text{ }^\circ\text{C}$ and (d) $T = 800 \text{ }^\circ\text{C}$ after N_2 annealing, where T_N of (c) and (d) is $1000 \text{ }^\circ\text{C}$ and $900 \text{ }^\circ\text{C}$, respectively, and t_N of (c) and (d) is 5 and 10 min, respectively. SiC dots show Moiré patterns interfered by SiC and Si double layers, as shown in Fig. 7. (a) at $T = 25 \text{ }^\circ\text{C}$ shows that some SiC dots are observed only near the Si surface, and the SiC dot density is very low at room temperature. On the other hand, the SiC dot density; the N of (b) and (c) are approximately 2.1×10^{12} and $1.6 \times 10^{12} \text{ cm}^{-2}$, respectively, and the average SiC dot size; R of (b) and (c) are approximately 3.7 and 2.9 nm, respectively. Thus, R decreases and N slightly decreases after N_2 annealing. On the other hand, (d) shows that $R \approx 6.3 \text{ nm}$ and $N \approx 7 \times 10^{11} \text{ cm}^{-2}$, and thus the SiC dot size increases and density decreases under high T condition.

dots shown as clear white dots are formed within an approximately 50 nm depth from the Si surface, and thus, SiC dot formation rate increases with increasing T . SiC dots in Figs. 5(b)–5(d) show a Moiré pattern interfered by two layers of SiC and Si, as discussed in Fig. 7. Average R of Figs. 5(b) and 5(c) are approximately 3.7 and 2.9 nm, respectively. The dot density; N of Figs. 5(b) and 5(c) in $150 \times 50 \text{ nm}^2$ area are approximately 2.1×10^{12} and $1.6 \times 10^{12} \text{ cm}^{-2}$, respectively. On the other hand, to evaluate the N_2 annealing effect on SiC dot formation, Figs. 5(c) and 5(d) show the TEM images at $T = 600 \text{ }^\circ\text{C}$ and $800 \text{ }^\circ\text{C}$ after N_2 annealing, respectively. Compared to Figs. 5(b), 5(c) indicates that the R and N decreases after N_2 annealing. Thus, the R decreases and N increases after N_2 annealing. On the other hand, Fig. 5(d) at $T = 800 \text{ }^\circ\text{C}$ shows that $R \approx 6.3 \text{ nm}$ and $N \approx 7 \times 10^{11} \text{ cm}^{-2}$, and thus the SiC dot size increases and density decreases under high T condition.

Here, we discuss the details of the SiC dot size distribution in the cross section area of depth (50 nm) \times lateral length (150 nm) Si layer except the SOX/Si interface. Figure 6(a) shows the histograms of long diameter of SiC size distributions, as the same data in Fig. 5(c), where $T = 600 \text{ }^\circ\text{C}$, $T_N = 1000 \text{ }^\circ\text{C}$, $t_N = 5 \text{ min}$, and $D_C = 4 \times 10^{16} \text{ cm}^{-2}$. The SiC dot size is normally distributed, resulting in $R \approx 2.9 \text{ nm}$ and σ_R (standard deviation of R) $\approx 1.1 \text{ nm}$. The SiC dot size distributions of Figs. 5(b) and 5(d) were also confirmed by the Gaussian distribution function. σ_R is almost independent of T and t_N . Figure 6(b) shows the T dependence of R (circles) and N (squares) before (dashed lines) and after N_2 annealing. The R increases monotonically with increasing T , but slightly decreases after N_2 annealing. Thus, the SiC dot grow largely during high T ion implantation process, but the SiC dot shrinks during high temperature N_2 annealing, which is possibly attributable to the C atom diffusion. On the other hand, the N decrease with increasing T , and thus, the N is the opposite T dependence of R . Therefore, it is required to optimize the process conditions of T and t_N to increase total

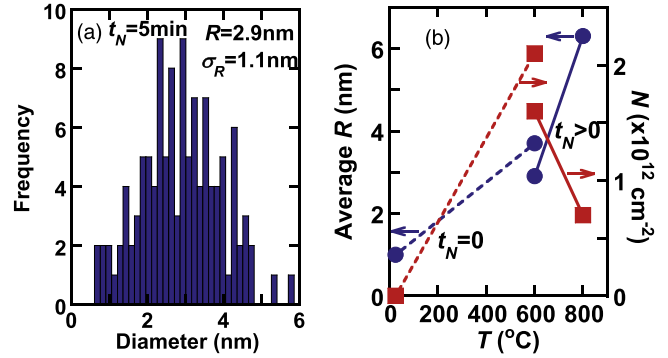


Fig. 6. (Color online) (a) Histogram of long diameter of SiC dots in cross section area of depth (50 nm) \times lateral length (150 nm) of Fig. 5(c), where $T = 600 \text{ }^\circ\text{C}$, $T_N = 1000 \text{ }^\circ\text{C}$, $t_N = 5 \text{ min}$, and $D_C = 4 \times 10^{16} \text{ cm}^{-2}$. R and σ_R are the average dot diameter ($\approx 2.9 \text{ nm}$) and the standard deviation ($\approx 1.1 \text{ nm}$), respectively. The statistical R distribution can be well fitted by Gaussian curve. (b) Average R (circles) and SiC dot density N (squares) versus T at the same data at Fig. 5, and the left and right vertical axes show average R and N , respectively. Solid and dashed lines show the data at $t_N > 0$ and $t_N = 0$, respectively. R increases monotonically with increasing T , but slightly decreases after N_2 annealing. On the other hand, N decrease with increasing T under $T \geq 600 \text{ }^\circ\text{C}$.

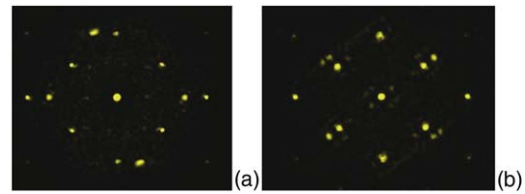


Fig. 7. (Color online) ED patterns of SiC dots in the Si layer, where $D_C = 4 \times 10^{16} \text{ cm}^{-2}$, $T = 800 \text{ }^\circ\text{C}$, $T_N = 900 \text{ }^\circ\text{C}$, and $t_N = 10 \text{ min}$. (a) and (b) show the interference ED patterns of cubic [110]3C-SiC and [110]Si double layers, and hexagonal [2 $\bar{1}$ $\bar{1}$ 0] H-SiC and [110] Si double layers, respectively.

SiC area S , since the S in Si layer is proportional to $\pi R^2 N / 4$. As a result, Fig. 6(b) shows that the maximum and minimum S in 1 cm^2 Si area are approximately 0.23 cm^2 before N_2 annealing and 0.11 cm^2 after N_2 annealing at $T = 600 \text{ }^\circ\text{C}$, and thus the area ratio of SiC dots to Si layer is lower than 1/4.

Next, we discuss the polytypes of SiC dots in Si layer. Figures 7(a) and 7(b) show the interference ED patterns of 3C-SiC/Si and H-SiC/Si double layers, respectively. We verified two types of SiC dot formation of 3C-SiC and H-SiC. Thus, the SiC-dots in the Si layer shown in Fig. 5 are confirmed by two polytypes of cubic- and hexagonal-SiC dots even in Si layer, similar to the results at SOX/Si interface shown in the next Fig. 8.

Secondly, we discuss the SiC dots at the SOX/Si interface. Figure 8(a) shows CSTEM images of a cross section of the C^+ -Si surface after N_2 annealing, and Figs. 8(b) and 8(c) show the typical ED patterns of cubic [110]3C-SiC corresponding to areas encircled in yellow in Fig. 8(a) and [2 $\bar{1}$ $\bar{1}$ 0] H-SiC corresponding to areas encircled in blue in Fig. 8(a), respectively, where $D_C = 4 \times 10^{16} \text{ cm}^{-2}$, $T = 800 \text{ }^\circ\text{C}$, $T_N = 900 \text{ }^\circ\text{C}$, and $t_N = 10 \text{ min}$. The lattice spot configuration of the SOX/Si interface is much different from the lattice spots of Si layer in Fig. 8(a). In addition, the ED patterns of Figs. 8(b) and 8(c) indicate that two different polytypes of 3C-SiC and H-SiC dots also coexist near the SOX/Si interface. Thus, CSTEM analysis can distinguished cubic SiC from hexagonal SiC, but it is

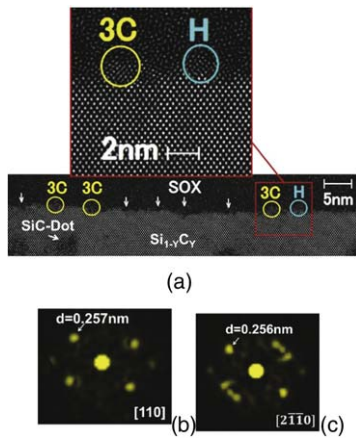


Fig. 8. (Color online) (a) CSTEM image of the cross section of C^+ -Si layer near the SOX/Si interface, where $D_C = 4 \times 10^{16} \text{ cm}^{-2}$, $T = 800 \text{ }^\circ\text{C}$, $T_N = 900 \text{ }^\circ\text{C}$, and $t_N = 10 \text{ min}$. The arrows shows the surface roughness which is possibly caused by the SiC dot formation. (b) and (c) show the ED patterns of cubic [110]SiC corresponding to area encircled in yellow in (a) and hexagonal [2 $\bar{1}$ 10] SiC corresponding to area encircled in blue in (a), respectively, where the diameter of all SiC dots in (a) is approximately 2 nm. (b) and (c) show that Si lattice space d at (220) 3C-SiC and (1011) H-SiC shown by arrows is approximately 0.257 and 0.256 nm, respectively.

difficult for the CSTEM to determine the specific polytypes of hexagonal SiC, such as 6H-SiC and 4H-SiC. The arrows of Fig. 8(a) suggest the possibility of the surface roughness caused by the SiC dot formation. As a result, the surface density of SiC dots are estimated at approximately $2 \times 10^{12} \text{ cm}^{-2}$, which is almost the same as that in the Si layer discussed in Figs. 5 and 6. The diameter of all SiC dots is approximately 2 nm. Namely, the SiC dots are grown into the SOX layer from the Si surface.

Next, we discuss the crystal quality of C^+ -Si layer evaluated by Raman spectroscopy, as a function of T and N_2 annealing. Figure 9(a) shows the t_N dependence of Raman spectra of Si-Si vibration, where $D_C = 4 \times 10^{16} \text{ cm}^{-2}$, $T = 600 \text{ }^\circ\text{C}$, $T_N = 1000 \text{ }^\circ\text{C}$, and the solid and dashed lines show the results at $t_N = 10$ and 0 min, respectively. Because of the Raman intensity improvement after N_2 annealing even at the penetration length of 8 nm in Si of 325 nm laser,³⁹⁾ Fig. 9(a) shows that the Si surface quality can be improved by N_2 annealing. Moreover, Fig. 9(b) shows the T dependence of the Si Raman intensity at $D_C = 4 \times 10^{16} \text{ cm}^{-2}$ and

$T_N = 1000 \text{ }^\circ\text{C}$, where the solid and dashed lines show the results at $t_N = 5 \text{ min}$ and 0, respectively. Even without N_2 annealing, when $T \geq 500 \text{ }^\circ\text{C}$, the Si Raman peak is observed even under high D_C condition of $4 \times 10^{16} \text{ cm}^{-2}$ and slightly increases with increasing T , which is the advantageous characteristic of hot- C^+ -ion implantation technique. However, when $T \leq 150 \text{ }^\circ\text{C}$, before N_2 annealing, the c-Si Raman peak was not observed, but the a-Si Raman peak of 480 cm^{-1} was observed, because of heavy C^+ -ion implantation induced damage in Si layer which leads to a-Si layer formation. On the other hand, even at $T \leq 150 \text{ }^\circ\text{C}$, the Si Raman peak is recovered after N_2 annealing, but is smaller than the maximum Si Raman intensity at $T \geq 500 \text{ }^\circ\text{C}$. Therefore, the combination processes of hot- C^+ -ion implantation and post N_2 annealing are strongly required to realize high crystal quality of heavy C^+ -Si layer.

On the other hand, very small TO mode^{19,28,40)} of Si-C vibration around 780 cm^{-1} was also observed shown in Fig. 9(c), similar to that of hot- C^+ -ion implanted a-Si,³⁸⁾ which is also the verification of SiC formation. However, the TO intensity is approximately 1/5 of Si-Si vibration intensity shown in Fig. 9(a), and is too small to evaluate the dependence of T and N_2 annealing effects on the crystal quality of SiC dots directly. Moreover, other Si-C vibration modes, such as LO mode around 970 cm^{-1} , were not observed, whereas we confirmed the C-C vibration modes of G and D bands which were already verified in C^+ -SOI and a-Si.^{31,38)} Thus, in this study, we indirectly discuss the crystal quality of SiC dots by using the Si-Si vibration results of Si layer embedding the SiC dots.

3.2. PL properties of C^+ -bulk-Si

3.2.1. PL components of four different SiC polytypes. TEM observations showed the successful formation of the different polytypes of cubic- and hexagonal-SiC dots in C^+ -bulk-Si. It is already reported that SiC has many polytypes with different exciton gap E_{GX} ($\approx E_G - 0.1 \text{ eV}$),^{19,28)} the hexagonality increases from 0% of 3C-SiC to 100% of 2H-SiC, and thus the E_{GX} also increases from 2.39 eV of 3C-SiC to 3.33 eV of 2H-SiC with increasing the hexagonality.^{19,28)} In this subsection, we discuss the broad PL properties of C^+ -bulk-Si which is possibly explained by the simple model for the sum of PL emissions by free exciton recombination from different

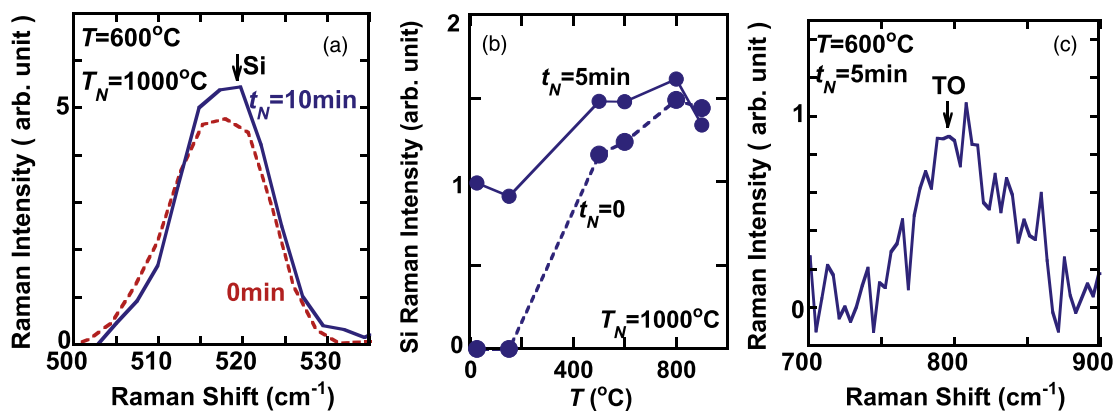


Fig. 9. (Color online) (a) t_N dependences of Raman spectrum of Si-Si vibration at $T = 600 \text{ }^\circ\text{C}$, (b) T dependence of Si Raman intensity around 520 cm^{-1} at $t_N = 5 \text{ min}$ (solid line) and 0 (dashed line), and (c) TO Raman spectrum of Si-C vibration at $T = 600 \text{ }^\circ\text{C}$ and $t_N = 5 \text{ min}$, where $D_C = 4 \times 10^{16} \text{ cm}^{-2}$ and $T_N = 1000 \text{ }^\circ\text{C}$. (a) shows that Raman intensity is improved after N_2 annealing. (b) shows that Si Raman intensity rapidly increases with increasing T , but is not observed under $T \leq 150 \text{ }^\circ\text{C}$ before N_2 annealing. TO Raman intensity of Si-C vibration in (c) is very low and approximately 1/5 of that of Si-Si vibration in (a).

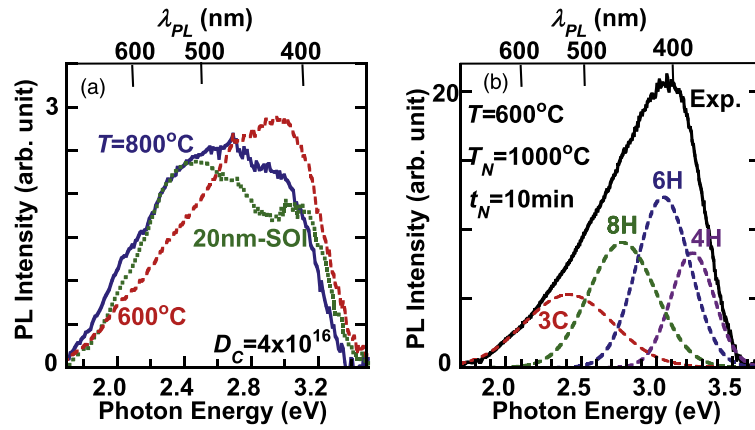


Fig. 10. (Color online) (a) PL spectra of C⁺-bulk-Si at $T = 800^\circ\text{C}$ (solid line) and 600°C (dashed line), compared with that of C⁺-SOI at $T = 800^\circ\text{C}$ (dotted line) before N₂ annealing ($t_N = 0$), where $D_C = 4 \times 10^{16} \text{ cm}^{-2}$. Lower and upper axes show the E_{PH} and λ_{PL} corresponding to E_{PH} , respectively. The I_{PL} of C⁺-bulk-Si is almost the same as that of C⁺-SOI, but the PL spectrum line shape of C⁺-bulk-Si depends on T . (b) PL component [Gaussian curve (dashed lines)] fittings for measured PL spectrum (solid lines), where $D_C = 4 \times 10^{16} \text{ cm}^{-2}$, $T = 600^\circ\text{C}$, $T_N = 1000^\circ\text{C}$, and $t_N = 10 \text{ min}$. Measured broad PL spectrum can be well fitted by four different SiC-polytypes of 3C-SiC ($I_{3\text{C}}$: red), 8H-SiC ($I_{8\text{H}}$: green), 6H-SiC ($I_{6\text{H}}$: blue), and 4H-SiC ($I_{4\text{H}}$: purple) whose exciton bandgap energies are each E_{GX} values ever reported.^{19,28)}

SiC-polytypes with different E_{GX} .^{19,28,37,38)} Thus in this study, we assume the typical SiC polytypes of 3C-, 8H-, 6H-, and 4H-SiC, considering the range and space of E_{GX} in SiC polytypes.^{37,38)}

Figure 10(a) shows the PL spectra of C⁺-bulk-Si at $T = 800^\circ\text{C}$ (solid line) and 600°C (dashed line), and 20 nm thick C⁺-SOI (dotted line) substrates before N₂ annealing, where $D_C = 4 \times 10^{16} \text{ cm}^{-2}$. We experimentally confirmed that PL intensities of C⁺-bulk-Si under both T conditions are almost the same as that of C⁺-SOI. However, the broad PL spectrum line shapes of C⁺-bulk-Si are much different from that of C⁺-SOI, and in addition, strongly depend on T . Moreover, Fig. 10(b) shows Gaussian curve (dashed lines) fittings of four PL components for measured PL spectrum (solid lines) after N₂ annealing, where $D_C = 4 \times 10^{16} \text{ cm}^{-2}$, $T = 600^\circ\text{C}$, $T_N = 1000^\circ\text{C}$, and $t_N = 10 \text{ min}$. Measured broad PL spectrum can be well fitted by the sum of PL emissions of four different SiC-polytype dots of 3C-SiC intensity ($I_{3\text{C}}$) with E_{GX} of 2.39 eV ($E_{3\text{C}}$), 8H-SiC intensity ($I_{8\text{H}}$) with E_{GX} of 2.74 eV ($E_{8\text{H}}$), 6H-SiC intensity ($I_{6\text{H}}$) with E_{GX} of 3.05 eV ($E_{6\text{H}}$), and 4H-SiC intensity ($I_{4\text{H}}$) with E_{GX} of 3.27 eV ($E_{4\text{H}}$)^{19,28)} both at the SOX/Si interface and in the Si layer. PL component of 2H-SiC with higher E_{GX} was not observed in this study. It was also verified that PL spectra of all process conditions in this study can be well fitted by four different polytypes of 3C-SiC to 4H-SiC dots. Consequently, measured PL spectrum as a function of photon energy E ; $I_{\text{PL}}(E)$ can be given by the following equation

$$I_{\text{PL}}(E) = \sum_{i=1}^4 N_i I_i^0(E) = N_{3\text{C}} I_{3\text{C}}^0(E) + N_{8\text{H}} I_{8\text{H}}^0(E) + N_{6\text{H}} I_{6\text{H}}^0(E) + N_{4\text{H}} I_{4\text{H}}^0(E), \quad (1)$$

where $N_{3\text{C}}$, $N_{8\text{H}}$, $N_{6\text{H}}$, and $N_{4\text{H}}$ are densities of 3C-, 8H-, 6H-, and 4H-SiC dots, respectively, and $I_{3\text{C}}^0$, $I_{8\text{H}}^0$, $I_{6\text{H}}^0$, and $I_{4\text{H}}^0$ are PL intensities per one dot of 3C-, 8H-, 6H-, and 4H-SiC, respectively.

In the following subsections, we discuss the process condition dependence of PL properties of C⁺-bulk-Si.

3.2.2. N₂ annealing effects. Next, we discuss the post N₂ annealing effects on PL properties.

Firstly, we discuss the t_N dependence of PL properties. Figure 11(a) shows the t_N dependence of PL spectrum at $T_N = 1000^\circ\text{C}$, $T = 600^\circ\text{C}$, and $D_C = 4 \times 10^{16} \text{ cm}^{-2}$, where PL intensity I_{PL} is normalized by the peak I_{PL} before N₂ annealing ($t_N = 0$). I_{PL} strongly depends on t_N , but the PL spectrum line shape keeps in the whole range of t_N . The I_{PL} enhancement factor at $T_N = 1000^\circ\text{C}$ rapidly increases to approximately 5.6 at $t_N = 5 \text{ min}$ and then slowly decreases with increasing t_N in $t_N > 5 \text{ min}$. Moreover, Fig. 11(b) shows the I_{PL} enhancement factors versus t_N at various T_N , where $T = 600^\circ\text{C}$ and $D_C = 4 \times 10^{16} \text{ cm}^{-2}$. At $T_N \geq 900^\circ\text{C}$, the peak- I_{PL} enhancement rapidly increases at $5 \leq t_N \leq 10 \text{ min}$, and the maximum I_{PL} enhancement factor increases with increasing T_N , although TEM observations shown in Figs. 5(b), 5(c), and 6(b) show that the SiC dot density decreases after N₂ annealing. Thus, the I_{PL} enhancement after N₂ annealing is possibly attributable to the PL intensity enhancement per one dot by the Si crystal quality improvement after N₂ annealing at high T_N , which is already discussed by the Raman intensity increase at $t_N = 5 \text{ min}$ shown in Fig. 9(b). However, in the case of $t_N > 5 \text{ min}$, the peak- I_{PL} enhancement ΔI_{PL} decreases with increasing t_N , and can be well fitted by the exponential decay function (dashed lines) with the correlation coefficient of greater than 0.98, as shown in Eq. (2), which is considered to be due to the SiC dot density N reduction in Eq. (1) during high T_N annealing, as shown as the t_N dependence of N in Fig. 6(b)

$$\Delta I_{\text{PL}}(t_N) = I_1 + I_2 \exp\left(-\frac{t_N}{t_D}\right), \quad (2)$$

where t_D indicates the time constant for decaying PL intensity due to the N reduction at T_N , $I_1 + I_2$ is a maximum PL intensity (I_{MAX}), and I_1 is a minimum PL intensity (I_{MIN}) at $t_N = \infty$. The fitting t_D at $T_N = 900^\circ\text{C}$ and 1000°C are approximately 30 min and 21 min, respectively, and thus the T_N dependence of t_D is small. Moreover, at $T_N = 1000^\circ\text{C}$, the peak- I_{PL} enhancement is nearly equal to zero at $t_N = 120 \text{ min}$, that is, the peak- I_{PL} value is almost the same as the initial peak- I_{PL} before N₂ annealing, because the large N -reduction

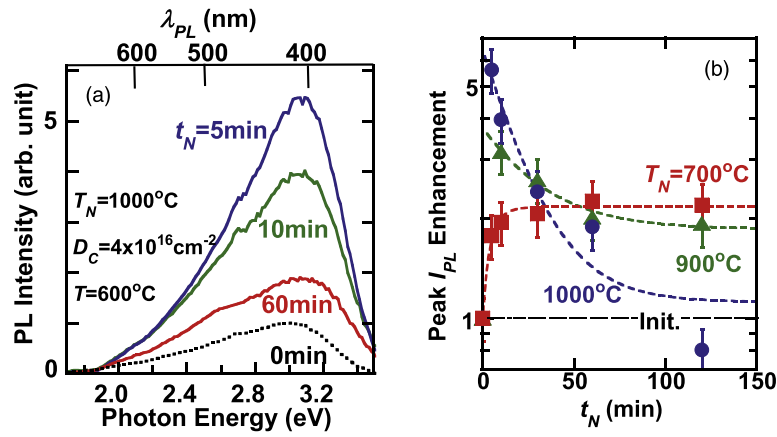


Fig. 11. (Color online) (a) t_N dependence of PL spectrum at $T_N = 1000^\circ\text{C}$, where $T = 600^\circ\text{C}$ and $D_C = 4 \times 10^{16}\text{cm}^{-2}$. I_{PL} is normalized by the peak I_{PL} before N_2 annealing ($t_N = 0$). I_{PL} strongly depends on t_N , but the PL spectrum line shape keeps in the whole range of t_N . Namely, the I_{PL} enhancement at $T_N = 1000^\circ\text{C}$ rapidly increases at $t_N = 5$ min and then slowly decreases with increasing t_N under $t_N > 5$ min (b) t_N dependence of peak- I_{PL} enhancement factors compared with the peak- I_{PL} at $t_N = 0$, as a parameter of T_N , where $T = 600^\circ\text{C}$ and $D_C = 4 \times 10^{16}\text{cm}^{-2}$. Under $t_N > 5$ min, the peak- I_{PL} enhancement slowly decreases with increasing t_N and can be well fitted by the exponential decay function of Eq. (2) (dashed line). However, in the case of low T_N of 700°C , the peak- I_{PL} enhancement factors (squares) continues increasing with increasing t_N , and saturates in $t_N > 30$ min, which can be well fitted by the exponential rise function of Eq. (3) (dashed line). The correlation coefficients of these fitting curves of Eqs. (2) and (3) are greater than 0.96.

possibly cancels out the Si crystal quality improvement during long N_2 annealing. On the other hand, at low T_N of 700°C , the peak- I_{PL} enhancement is relatively small compared with that at $T_N \geq 900^\circ\text{C}$, continues increasing with increasing t_N , and finally saturates even at long t_N . The small peak- I_{PL} enhancement in a short t_N is possibly attributable to the small recovery of Si crystal quality at low T_N . In addition, the peak- I_{PL} enhancement ΔI_{PL} at low T_N of 700°C can be well fitted by the following exponential rise function of Eq. (3) (dashed line) with the correlation coefficient of 0.99, which is considered to be due to a time scale t_R of the recovery of Si crystal quality after low T_N annealing

$$\Delta I_{PL}(t_N) = I_3 + I_4 \left\{ 1 - \exp\left(-\frac{t_N}{t_R}\right) \right\}, \quad (3)$$

where I_3 is an initial PL intensity, and $I_3 + I_4$ is the maximum PL intensity. The time scale of the Si quality recovery t_R was very short and approximately 5 min at $T = 700^\circ\text{C}$. Furthermore, the fitting I_{MAX} of Eqs. (2) and (3) gradually increases from 2.2 to 6.4 with increasing T_N from 700°C to 1000°C .

Next, we discuss the t_N dependences of PL components at high T_N of 1000°C . Figure 12(a) shows the t_N dependences of the peak- I_{PL} of main cubic and hexagonal PL components of I_{3C} (circles) and I_{6H} (rhombi), and Fig. 12(b) shows E_{4H} (triangles), E_{6H} (rhombi), E_{8H} (squares), and E_{3C} (circles) as a function of t_N , where $T = 600^\circ\text{C}$, $T_N = 1000^\circ\text{C}$, and $D_C = 4 \times 10^{16}\text{cm}^{-2}$. Both PL component intensities rapidly increase at $t_N = 5$ min, and decrease with increasing t_N at $t_N > 5$ min, which can be well fitted by the exponent decay function of Eq. (2) (dashed lines). Thus, the t_N dependence of I_{3C} and I_{6H} is almost the same as that of I_{PL} enhancement at $T_N = 1000^\circ\text{C}$ in Fig. 11(b). Therefore, the physical mechanism for the t_N dependence of I_{PL} components is the same as that for the t_N dependence of I_{PL} enhancement discussed in Fig. 11(b). Namely, the rapid I_{PL} component increase at short N_2 annealing is probably due to the Si crystal quality improvement shown as the Raman intensity versus t_N in Fig. 9(b). On the other hand, the I_{PL} component reduction at long N_2 annealing is probably attributable to the SiC dot

density reduction during high temperature N_2 annealing at $T_N = 1000^\circ\text{C}$, as discussed as the SiC dot density decrease under high T conditions shown in Fig. 6(b). On the other hand, Fig. 12(b) shows that all peak PL energies of PL components is independent of t_N , and is almost the same as reference E_{GX} of four different polytypes of 3D-SiC [dashed lines in Fig. 12(b)].^{19,28}

Secondly, we discuss the T_N dependence of PL properties. Figure 13(a) shows the T_N dependence of PL spectrum, where the dotted line shows the PL spectrum before N_2 annealing, $T = 600^\circ\text{C}$, $t_N = 10$ min, and $D_C = 4 \times 10^{16}\text{cm}^{-2}$. The I_{PL} drastically increases with increasing T_N at $T_N \leq 1000^\circ\text{C}$, which is possibly attributable to the Si crystal quality recovery, as shown in Fig. 9(b). On the other hand, at $T_N = 1200^\circ\text{C}$, the I_{PL} rapidly decreases, which is possibly caused by the SiC dot density reduction after high T_N annealing shown in Fig. 6(b). However, the PL spectrum line shape is almost independent of T_N , except $T_N = 1200^\circ\text{C}$ data. Moreover, Fig. 13(b) shows the T_N dependence of the peak- I_{PL} of main cubic and hexagonal PL components of I_{3C} (circles) and I_{6H} (rhombi) as well as I_{MAX} (triangles). I_{MAX} , peak- I_{6H} , and peak- I_{3C} have the maximum values at $T_N \approx 900^\circ\text{C}$ – 1000°C , but only at $T_N = 1200^\circ\text{C}$, I_{3C} component is higher than I_{6H} component. Similar to Fig. 12(b), all E_{GX} of four PL components was almost independent of T_N , and was nearly equal to reference E_{GX} of four different polytypes of 3D-SiC.^{19,28}

Here, we estimate the total photon emission number from each PL component shown in Fig. 10(b), which is an indicator for each polytype formation ratio of SiC dots. The ratio of one PL component I_I to total I_{PL} emission; P_I (subscript I is from 3C to 4H) can be precisely determined by the integrated I_I divided by the total integrated I_{PL} in the whole range of photon energy E .^{37,38} Namely

$$P_I = \frac{\int I_I(E)dE}{\int I_{PL}(E)dE}. \quad (4)$$

Figure 14 shows the T_N dependence of integrated PL component ratios of Eq. (4), where $T = 600^\circ\text{C}$, $t_N = 10$ min

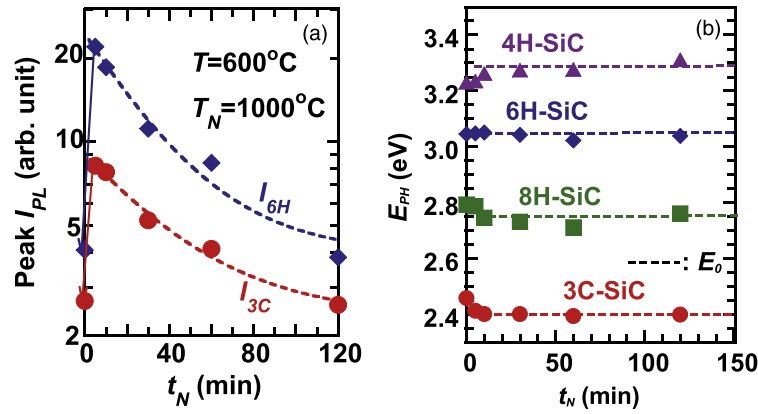


Fig. 12. (Color online) t_N dependences of (a) main hexagonal and cubic PL components of peak- I_{6H} (rhombi) and peak- I_{3C} (circles), and (b) E_{6H} (triangles), E_{6H} (rhombi), E_{8H} (squares), and E_{3C} (circles), where $T = 600^\circ\text{C}$, $T_N = 1000^\circ\text{C}$, and $D_C = 4 \times 10^{16}\text{ cm}^{-2}$. Dashed lines in (a) show the fitting curves of exponent decay function of Eq. (2) with the correlation coefficients of 0.99. Dashed lines in (b) show reference E_{GX} of four different SiC polytypes.^{19,28} (a) shows that all peak PL intensities rapidly increase at $t_N = 5$ min, and then decrease with increasing t_N . However, (b) shows that each peak E_{PH} is almost the same as experimental E_{GX} (E_0) and independent of t_N within 0.1 eV.

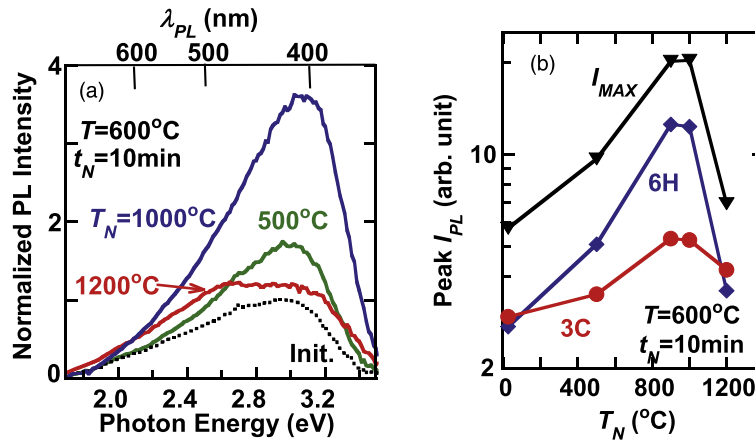


Fig. 13. (Color online) T_N dependence of (a) PL spectrum, and (b) I_{MAX} (triangles), peak- I_{6H} (rhombi), and peak- I_{3C} (circles), where $T = 600^\circ\text{C}$, $t_N = 10$ min, and $D_C = 4 \times 10^{16}\text{ cm}^{-2}$. (a) shows that the PL spectrum strongly depends on T_N . (b) shows that I_{MAX} , peak- I_{6H} , and peak- I_{3C} have the maximum values at $T_N \approx 900^\circ\text{C} - 1000^\circ\text{C}$.

and $D_C = 4 \times 10^{16}\text{ cm}^{-2}$. All PL emission component strongly depends on T_N . For example, total hexagonal PL component ratio is the main component and higher than 70% at $500^\circ\text{C} < T_N \leq 1000^\circ\text{C}$, but the P_{3C} is the main component of approximately 50% at $500^\circ\text{C} > T_N$ and $T_N > 1000^\circ\text{C}$. The T_N dependence difference of P_I between the cubic and hexagonal polytypes of SiC is probably the formation rate difference between the cubic and hexagonal polytypes of SiC at T_N .

3.2.3. Hot-C⁺-ion implantation temperature dependence. In this subsection, we discuss the hot-C⁺-ion implantation temperature T dependence of PL properties of SiC dots.

Figures 15(a) and 15(b) show the T dependence of PL spectra at $t_N = 0$ and $t_N = 5$ min, respectively, where $T_N = 1000^\circ\text{C}$ and $D_C = 4 \times 10^{16}\text{ cm}^{-2}$. The I_{PL} value and PL spectrum line shape strongly depend on T , which is also affected by N_2 annealing. Although Fig. 9(b) shows that the crystal Si layer is amorphized after C⁺ ion implantation at $T = 25^\circ\text{C}$ before N_2 annealing, Fig. 15(a) shows that normal PL emission was experimentally confirmed even at $T = 25^\circ\text{C}$ before N_2 annealing, but the PL spectrum line shape with low PL intensity at higher photon energy is much different from those at $T \geq 600^\circ\text{C}$, because of no I_{4H} around 3.3 eV of

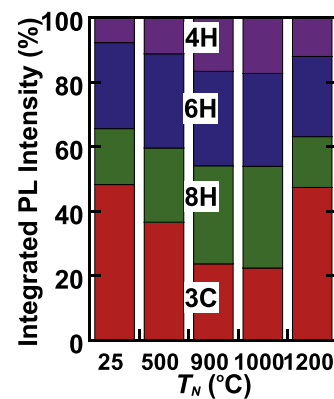


Fig. 14. (Color online) T_N dependence of integrated PL component ratios of Eq. (4) which are proportional to total PL photon emission numbers from each SiC polytype, where $T = 600^\circ\text{C}$, $t_N = 10$ min and $D_C = 4 \times 10^{16}\text{ cm}^{-2}$. All PL emission components strongly depend on T_N . The hexagonal PL components are the main component at $500^\circ\text{C} \leq T_N \leq 1000^\circ\text{C}$, but the P_{3C} is the main component at $500^\circ\text{C} > T_N$ and $T_N > 1000^\circ\text{C}$.

photon energy. Therefore, it is possible that SiC dots are formed even in an amorphous Si.^{37,38} After N_2 annealing, Fig. 15(b) shows that I_{PL} is enhanced by approximately four factors under all T conditions. Especially at $T = 25^\circ\text{C}$, the I_{PL}

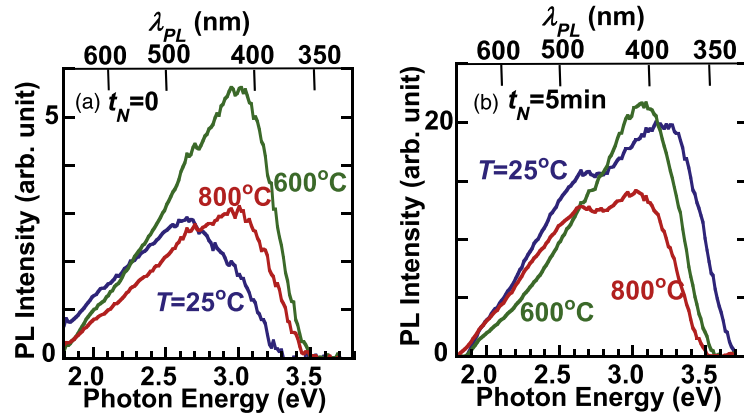


Fig. 15. (Color online) T dependence of PL spectra at (a) $t_N = 0$ and (b) $t_N = 5$ min, where $T_N = 1000^\circ\text{C}$ and $D_C = 4 \times 10^{16} \text{ cm}^{-2}$. I_{PL} value and PL spectrum line shape strongly depend on T , which is also affected by N_2 annealing.

enhancement is very large in the UV range of I_{4H} , and thus, the PL spectrum line shape is changed after N_2 annealing.

Secondly, we discuss the T dependence of PL components of SiC dots.

Figure 16(a) shows the T dependence of the peak- I_{PL} of main cubic and hexagonal PL components of 3C- (circles) and 6H-SiC (rhombi) at $T_N = 1000^\circ\text{C}$ and $D_C = 4 \times 10^{16} \text{ cm}^{-2}$, where the solid and dashed lines show the data at $t_N = 5$ min and 0, respectively. The peak- I_{6H} at $t_N = 5$ min has the double peaks at $T = 25^\circ\text{C}$ and 600°C , but the peak- I_{6H} at $t_N = 0$ has the single peak at $T = 600^\circ\text{C}$. On the other hand, the peak- I_{3C} at $t_N = 5$ min has the peak at room temperature and the minimum at $T = 500^\circ\text{C}$, and then continues increasing with increasing T at $T \geq 500^\circ\text{C}$. Therefore, Fig. 16(a) indicates that the optimum T is around 600°C to improve I_{6H} . In addition, Fig. 16(b) shows the T dependence of peak PL component enhancement factors at $t_N = 5$ min of I_{4H} (triangles), I_{6H} (rhombi), I_{8H} (squares), and I_{3C} (circles), compared with each peak- I_{PL} at $t_N = 0$, where $T_N = 1000^\circ\text{C}$ and $D_C = 4 \times 10^{16} \text{ cm}^{-2}$. The PL intensity enhancement factors after N_2 annealing are larger than 3 in the whole range of T , and rapidly increases with decreasing T at $T \leq 500^\circ\text{C}$. Large I_{PL} enhancement at low T is possibly due to the Si crystal quality improvement after N_2 annealing as well as the SiC dot density increase with decreasing T shown in Fig. 6(b). In addition, the peak- I_{PL} enhancement factors increase with increasing the hexagonality, and for example the I_{4H} enhancement factor reaches over 60, whose physical mechanism is not understood at present.

Finally, Figs. 17(a) and 17(b) show the T dependence of the ratio of P_{4H} , P_{6H} , P_{8H} , and P_{3C} of Eq. (4) at $t_N = 0$ and 5 min, respectively, where $T_N = 1000^\circ\text{C}$, $t_N = 5$ min and $D_C = 4 \times 10^{16} \text{ cm}^{-2}$. The ratio of each PL component strongly depends on T , but the T dependence is much affected by N_2 annealing. P_{6H} and P_{8H} ratios are approximately 30%, and almost independent of T , which is not affected by N_2 annealing. On the other hand, P_{3C} and P_{4H} ratios are much affected by N_2 annealing. Before N_2 annealing, Fig. 17(a) shows that P_{3C} ratio is very high, but P_{4H} is very low at $T \leq 150^\circ\text{C}$. However, after N_2 annealing, P_{4H} increases with decreasing T , but P_{3C} has the minimum at $T \approx 800^\circ\text{C}$. Therefore, the PL component ratios are partially controlled by T and N_2 annealing.

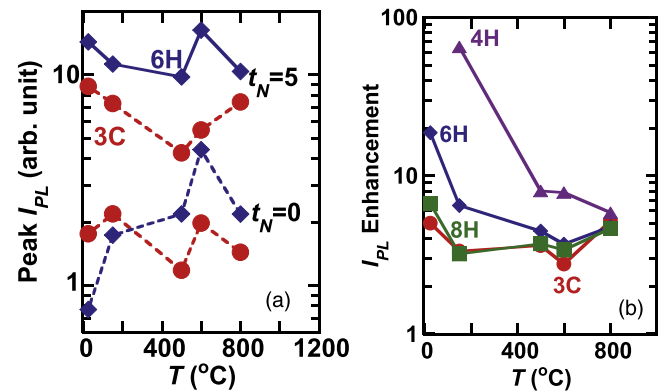


Fig. 16. (Color online) T dependence of (a) main hexagonal and cubic PL components of peak- I_{6H} (rhombi) and peak- I_{3C} (circles), and (b) peak- I_{PL} enhancement factors of I_{4H} (triangles), I_{6H} (rhombi), I_{8H} (squares), and I_{3C} (circles) at $t_N = 5$ min compared with peak- I_{PL} at $t_N = 0$, where $T_N = 1000^\circ\text{C}$ and $D_C = 4 \times 10^{16} \text{ cm}^{-2}$. Solid and dashed lines in (a) show the data at $t_N = 5$ min and 0, respectively. (a) shows that the T dependence of peak- I_{6H} is different from that of peak- I_{3C} , which also depends on N_2 annealing. (b) shows that the PL intensity enhancement factors after N_2 annealing rapidly increase with decreasing T at $T \leq 500^\circ\text{C}$, which is enhanced with increasing the hexagonality.

3.2.4. C^+ -ion dose dependence. In this subsection, we discuss the D_C dependence of PL properties of SiC dots.

Figure 18 shows the D_C dependence of PL spectrum at $T = 800^\circ\text{C}$ after N_2 annealing, where $T_N = 1000^\circ\text{C}$ and $t_N = 5$ min. Both PL intensity and PL spectrum line shape strongly depend on D_C . Especially, the PL spectrum line shape at $D_C = 1 \times 10^{16} \text{ cm}^{-2}$ shows lower I_{PL} at lower photon energy region around 2.4 eV, and thus is much different from that with double PL peaks at $D_C \geq 4 \times 10^{16} \text{ cm}^{-2}$, which is attributable to the strong D_C dependence of PL components, as discussed in Fig. 19(a).

Figure 19(a) shows the D_C dependence of peak values of PL components of I_{4H} (triangles), I_{6H} (rhombi), I_{8H} (squares), and I_{3C} (circles) at $t_N = 5$ min, and Fig. 19(b) shows the FWHM of Si Raman peak at $t_N = 5$ min (solid line) and 0 (dashed line) as a function of D_C , where $T = 800^\circ\text{C}$ and $T_N = 1000^\circ\text{C}$. Figure 19(a) shows that peak I_{3C} and I_{8H} continue increasing with increasing D_C , and the peak- I_{3C} at $D_C = 6 \times 10^{16} \text{ cm}^{-2}$ is approximately 23 times as large as that at $D_C = 1 \times 10^{16} \text{ cm}^{-2}$, whereas the peak I_{6H} and I_{4H} have the maximum value at $D_C = 4 \times 10^{16}$ and $2 \times 10^{16} \text{ cm}^{-2}$, respectively. Thus, PL components have the

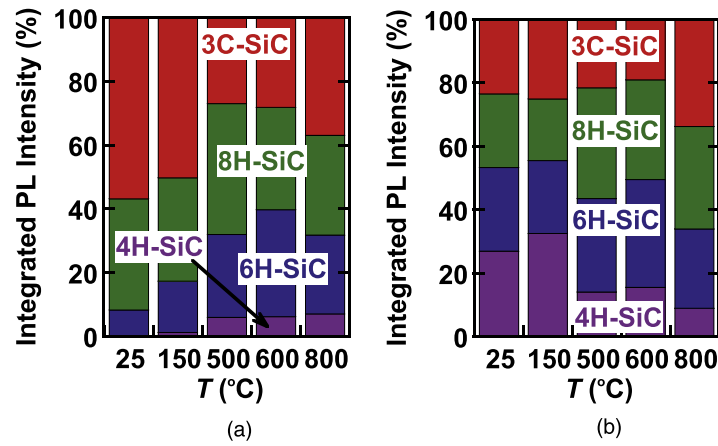


Fig. 17. (Color online) T dependence of the ratio of integrated PL intensities of each PL component; P_{4H} , P_{6H} , P_{8H} , and P_{3C} of Eq. (4) at (a) $t_N = 0$ and (b) 5 min, where $T_N = 1000$ °C and $D_C = 4 \times 10^{16}$ cm $^{-2}$. T dependence of the ratio of integrated PL intensities of each PL component strongly depends on t_N . Especially, the T and N_2 annealing influences on P_{4H} and P_{3C} ratios are very large.

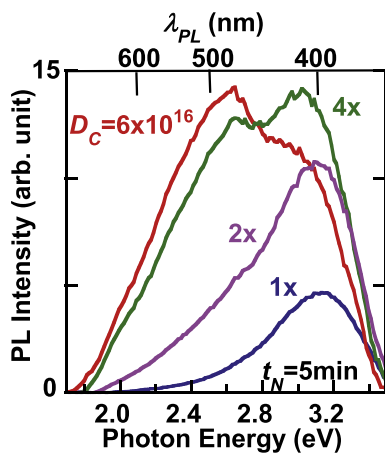


Fig. 18. (Color online) D_C dependence of PL spectrum, where $T = 800$ °C, $T_N = 1000$ °C, and $t_N = 5$ min. Both PL intensity and PL spectrum line shape strongly depend on D_C .

different D_C dependence, which leads to the strong D_C dependence of the PL spectrum line shape, as shown in Fig. 18. Figure 19(b) shows that the FWHM of Si Raman peak is almost independent of D_C within 8%, which indicates that the Si crystal quality was not degraded by high D_C in this study. As a result, the PL component increase with increasing

D_C is possibly caused by the SiC dot density increase with increasing D_C .

Finally, Fig. 20 shows the D_C dependence of the ratio of integrated PL intensities of each PL component; P_{4H} , P_{6H} , P_{8H} , and P_{3C} of Eq. (4), where $T = 800$ °C, $T_N = 1000$ °C, and $t_N = 5$ min. With increasing D_C , P_{4H} decreases, but P_{3C} increases, whereas P_{6H} , and P_{8H} are almost independent of D_C . Therefore, a cubic SiC dot formation rate increases with increasing D_C , but on the contrary, 4H-SiC dot formation rate becomes high under low D_C condition and other hexagonal dot formation of 8H- and 6H-SiC is almost independent of D_C . Thus, it is possible for D_C to control the SiC polytypes partially.

4. Conclusion

We experimentally studied SiC nano-dot formation in a bulk-Si substrate for a future Si-photonic device, using the very simple processes of a hot-C $^{+}$ -ion implantation into (100) bulk-Si substrate at substrate temperature T and the following N_2 annealing in various annealing temperature T_N for annealing time t_N , where $1 \times 10^{16} \leq D_C \leq 6 \times 10^{16}$ cm $^{-2}$, 25 °C $\leq T \leq 800$ °C, 500 °C $\leq T_N \leq 1200$ °C, and $0 \leq t_N \leq 120$ min. We demonstrated very large PL intensity in the wide range of near-UV/visible regions from 2–6 nm diameter SiC dots in the C $^{+}$ -Si layer evaluated by CSTEM

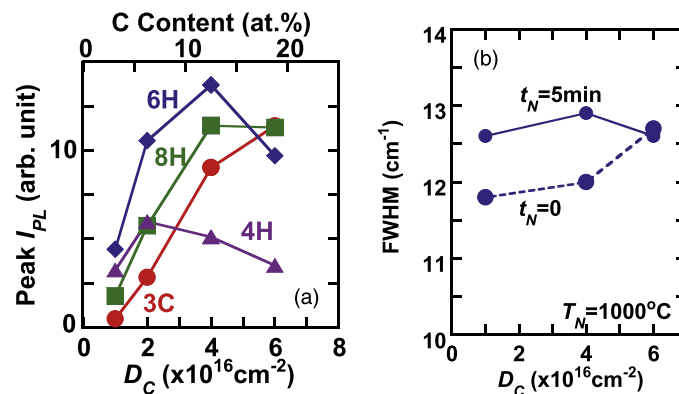


Fig. 19. (Color online) D_C dependence of (a) peak values of I_{4H} (triangles), I_{6H} (rhombi), I_{8H} (squares), and I_{3C} (circles) at $t_N = 5$ min, and (b) FWHM of Si Raman peak at $t_N = 5$ min and 0, where $T = 800$ °C and $T_N = 1000$ °C. (a) shows that peak I_{3C} and I_{8H} continue increasing with increasing D_C , but peak I_{6H} and I_{4H} have the maximum values at $D_C = 4 \times 10^{16}$ and 2×10^{16} cm $^{-2}$, respectively. (b) shows that FWHM is almost independent of D_C within 8%.

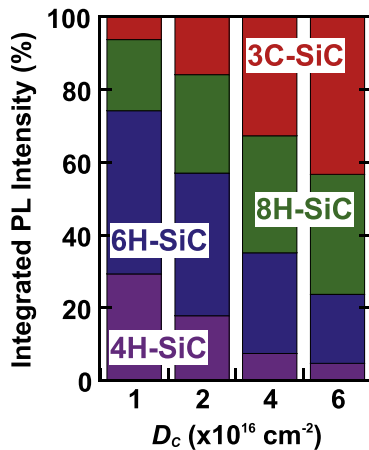


Fig. 20. (Color online) D_C dependence of the ratio of integrated PL intensities of each PL component; P_{4H} , P_{6H} , P_{8H} , and P_{3C} of Eq. (4), where $T = 800 \text{ }^\circ\text{C}$, $T_N = 1000 \text{ }^\circ\text{C}$, and $t_N = 5 \text{ min}$. With increasing D_C , P_{4H} decreases, but P_{3C} increases, whereas P_{6H} , and P_{8H} are almost independent of D_C .

observation, and the PL intensity is almost the same as that from the SiC dots in C^+ -SOI substrate.

The C atom depth profile, evaluated by C1s spectrum of XPS for C^+ -bulk-Si, shows small C segregation at the SOX/Si interface and wide C content depth profile, whose peak C content at SOX/Si interface slightly increases with increasing T . CSTEM observation shows that there are two types of SiC dots with cubic and hexagonal polytypes in C^+ -bulk Si layer. It is also verified that 3C/H-SiC dots with an approximately 2 nm diameter R grow toward a SOX layer from the Si surface. As a result, the statistical R distribution in the Si layer is Gaussian type, and the average R decreases from approximately 1–6 nm with decreasing T and increasing t_N , whereas the standard deviation of R is kept 1.1 nm. Moreover, the SiC dot density in the Si layer is approximately $1.5 \times 10^{12} \text{ cm}^{-2}$ and also decreases with increasing T and t_N . UV-Raman spectroscopy of Si–Si vibration of C^+ -Si layer suggests that C^+ -Si layer quality is improved by increasing T and short N_2 annealing.

We successfully observe very strong and broad PL intensity I_{PL} after N_2 annealing in the wide range of T (from room temperature to $800 \text{ }^\circ\text{C}$). The broad PL spectrum can be well fitted by different PL components of four SiC-polytypes of cubic and hexagonal SiC dots with different exciton bandgap E_{GX} (3C-, 8H-, 6H- and 4H-SiC). The PL spectrum line shape and I_{PL} strongly depends on process conditions of T , T_N , t_N , and D_C , which is possibly attributable to the difference of the process conditions for each SiC polytype formation.

Optimum process conditions exist for improving I_{PL} by improving the C^+ -Si layer quality and enlarging the total area of SiC dots fabricated in C^+ -Si layer. For example, optimum T , T_N , and D_C for enlarging I_{PL} are approximately $600 \text{ }^\circ\text{C}$, $1000 \text{ }^\circ\text{C}$, and $4 \times 10^{16} \text{ cm}^{-2}$, respectively. However, optimum process conditions for improving each PL component are much different between each PL component, especially, the process condition dependence of I_{3C} component is much different from that of I_{4H} component. Thus, it is partially possible to control the PL spectrum line shape by optimizing the process conditions for C^+ -bulk Si.

Consequently, the ULSI compatible technique of SiC-dot formation in C^+ -bulk-Si substrate is very promising for future electron and photonic hybrid Si-devices.

Acknowledgments

This work was partially supported by a Grant-in-Aid for Scientific Research from the Japan Society for the Promotion of Science (17K06359).

- 1) S. Saito et al., *Jpn. J. Appl. Phys.* **45**, L679 (2006).
- 2) S. Saito et al., *IEDM Tech. Dig.*, 2008, p. 19.5.
- 3) L. Pavesi and D. J. Lockwood, *Silicon Photonics* (Springer, Berlin, 2004).
- 4) T. Mizuno, K. Tobe, Y. Maruyama, and T. Sameshima, *Jpn. J. Appl. Phys.* **51**, 02BC03 (2012).
- 5) T. Mizuno, T. Aoki, Y. Nagata, Y. Nakahara, and T. Sameshima, *Jpn. J. Appl. Phys.* **52**, 04CC13 (2013).
- 6) T. Mizuno, Y. Nakahara, Y. Nagata, Y. Suzuki, T. Aoki, and T. Sameshima, *Jpn. J. Appl. Phys.* **53**, 04EC08 (2014).
- 7) T. Mizuno, Y. Nagata, Y. Suzuki, Y. Nakahara, T. Aoki, and T. Sameshima, *Jpn. J. Appl. Phys.* **53**, 04EC09 (2014).
- 8) T. Mizuno, Y. Nagamine, Y. Suzuki, Y. Nakahara, Y. Nagata, T. Aoki, and T. Sameshima, *Jpn. J. Appl. Phys.* **54**, 04DC05 (2015).
- 9) T. Mizuno, Y. Suzuki, Y. Nagamine, Y. Nakahara, Y. Nagata, T. Aoki, and T. Maeda, *Jpn. J. Appl. Phys.* **54**, 04DC02 (2015).
- 10) L. Donetti, F. Gámiz, J. B. Roldán, and A. Godoy, *J. Appl. Phys.* **100**, 013701 (2006).
- 11) K. Uchida, H. Watanabe, A. Kinoshita, J. Koga, T. Numata, and S. Takagi, *IEDM Tech. Dig.*, 2002, p. 47.
- 12) K. Uchida, J. Koga, and S. Takagi, *J. Appl. Phys.* **102**, 074510 (2007).
- 13) G. Tsutsui, M. Saitoh, and T. Hiramoto, *IEEE Trans. Electron Devices* **26**, 836 (2005).
- 14) B. K. Agrawal and S. Agrawal, *Appl. Phys. Lett.* **77**, 3039 (2000).
- 15) S. S. Iyer and Y.-H. Xie, *Science* **260**, 40 (1993).
- 16) L. R. Tessler and I. Solomon, *Phys. Rev. B* **52**, 10962 (1995).
- 17) W. Liu, M. Zhang, C. Lin, Z. Zeng, L. Wang, and P. K. Chu, *Appl. Phys. Lett.* **78**, 37 (2001).
- 18) S. T. Pantelides and S. Zollner, *Silicon–Germanium Carbon Alloys* (Taylor & Francis, New York, 2002).
- 19) J. Fan and P. K. Chu, *Silicon Carbide Nanostructure* (Springer, Cham, 2014), Chap. 3–5.
- 20) K. Adhikari and A. K. Ray, *J. Nanopart. Res.* **14**, 816 (2012).
- 21) S. Kim, J. E. Spanter, and I. P. Herman, *Jpn. J. Appl. Phys.* **39**, 5875 (2000).
- 22) T. V. Torchynska, A. D. Canoa, S. J. Sandoval, M. Dybicz, S. Ostapenkoc, and M. Mynbaevad, *Microelectron. J.* **36**, 536 (2005).
- 23) S. Lin, S. Zhang, X. Li, W. Xu, X. Pi, X. Liu, F. Wang, H. Wu, and H. Chen, *J. Phys. Chem. C* **119**, 19772 (2015).
- 24) E. Bekaroglu, M. Topsakal, S. Cahangirov, and S. Ciraci, *Phys. Rev. B* **81**, 075433 (2010).
- 25) G. Wei, W. Qin, G. Wang, J. Sun, J. Lin, R. Kim, D. Zhang, and K. Zheng, *J. Phys. D: Appl. Phys.* **41**, 235102 (2008).
- 26) J. A. Borders, S. T. Picraux, and W. Beezhold, *App. Phys. Lett.* **18**, 509 (1971).
- 27) Y. H. Gao, Z. Zhang, L. S. Liao, and X. M. Bao, *App. Phys. Lett.* **66**, 2382 (1995).
- 28) T. Kimoto and J. A. Cooper, *Fundamentals of Silicon Carbide Technology* (IEEE Press, Singapore, 2014), Chap. 2., Chap. 5.
- 29) T. Kimoto, S. Nakazawa, K. Hashimoto, and H. Matsunami, *Appl. Phys. Lett.* **79**, 2761 (2001).
- 30) T. Mizuno, Y. Nagamine, Y. Omata, Y. Suzuki, W. Urayama, T. Aoki, and T. Sameshima, *Jpn. J. Appl. Phys.* **55**, 04EB02 (2016).
- 31) T. Mizuno, Y. Omata, Y. Nagamine, T. Aoki, and T. Sameshima, *Jpn. J. Appl. Phys.* **56**, 04CB03 (2017).
- 32) T. Mizuno, Y. Omata, S. Nakada, T. Aoki, and T. Sasaki, *Int. Conf. on Solid State Devices and Materials 2017: Extended Abstract of Solid State Devices and Materials* (Sendai, Japan, 2017) (The Japan Society of Applied Physics, Tokyo, 2017), p. 537.
- 33) T. Mizuno, Y. Omata, R. Kanazawa, Y. Iguchi, S. Nakada, T. Aoki, and T. Sasaki, *Jpn. J. Appl. Phys.* **57**, 04FB03 (2018).
- 34) Y. Shimizu et al., *Appl. Phys. Lett.* **98**, 232101 (2011).
- 35) Y. Shimizu, H. Takamizawa, K. Inoue, F. Yano, S. Kudo, A. Nishida, T. Toyama, and Y. Nagai, *Jpn. J. Appl. Phys.* **55**, 026501 (2016).
- 36) T. Mizuno, S. Nakada, M. Yamamoto, S. Irie, Y. Omata, T. Aoki, and T. Sameshima, *Int. Conf. on Solid State Devices and Materials 2017*:

- Extended Abstract of Solid State Devices and Materials (Sendai, Japan, 2017) (The Japan Society of Applied Physics, Sendai, 2017), p. 597.
- 37) T. Mizuno, S. Nakada, M. Yamamoto, S. Irie, T. Aoki, and T. Sameshima, *Abstract of IEEE Silicon Nanoelectronics Workshop 2018* (IEEE, Honolulu, 2018), p. 121.
- 38) T. Mizuno, R. Kanazawa, Y. Omata, T. Aoki, and T. Sameshima, *Jpn. J. Appl. Phys.* **58**, SSBJ01 (2019).
- 39) S. M. Sze and K. K. Ng, *Physics of Semiconductor Devices* (Wiley, New York, 2007), Chap. 1.
- 40) D. N. Talwar and Z. C. Feng, *Comput. Mater. Sci.* **30**, 419 (2004).